frontiers | Frontiers in Environmental Science

TYPE Original Research
PUBLISHED 11 May 2023
DOI 10.3389/fenvs.2023.1180229

OPEN ACCESS

EDITED BY
Ahmed El Nemr,
National Institute of Oceanography and Fisheries (NIOF), Egypt

REVIEWED BY
Qazi Inamur Rahman,
Integral University, India
Muneeswaran Thillaichidambaram,
University of Chile, Chile
Ganapathi Raman,
Saveetha engineering college, India

*CORRESPONDENCE
Walid Nabgan,
walid.nabgan@urv.cat
Muhammad Ikram,
dr.muhammadikram@gcu.edu.pk
Anwar Ul-Hamid,
anwar@kfupm.edu.sa

RECEIVED 05 March 2023
ACCEPTED 12 April 2023
PUBLISHED 11 May 2023

CITATION
Zubair Arshad HM, Imran M, Haider A, Shahzadi I, Mustajab M, Ul-Hamid A, Nabgan W, Medina F, Aslam S and Ikram M (2023), Dye degradation, antimicrobial activity, and molecular docking analysis of carbon sphere and graphene oxide–doped aluminum oxide. *Front. Environ. Sci.* 11:1180229. doi: 10.3389/fenvs.2023.1180229

Dye degradation, antimicrobial activity, and molecular docking analysis of carbon sphere and graphene oxide–doped aluminum oxide

Hafiz Muhammad Zubair Arshad[1], Muhammad Imran[1], Ali Haider[2], Iram Shahzadi[3], Muhammad Mustajab[4], Anwar Ul-Hamid[5]*, Walid Nabgan[6]*, Francisco Medina[6], Sadaf Aslam[7] and Muhammad Ikram[4]*

[1]Department of Chemistry, Government College University Faisalabad, Sahiwal, Pakistan, [2]Department of Clinical Sciences, Faculty of Veterinary and Animal Sciences, Muhammad Nawaz Shareef University of Agriculture, Multan, Punjab, Pakistan, [3]Punjab University College of Pharmacy, University of the Punjab, Lahore, Pakistan, [4]Solar Cell Applications Research Lab, Department of Physics, Government College University Lahore, Lahore, Punjab, Pakistan, [5]Core Research Facilities, King Fahd University of Petroleum and Minerals, Dhahran, Saudi Arabia, [6]Departament d'Enginyeria Química, Universitat Rovira i Virgili, Tarragona, Spain, [7]Department of Veterinary Surgery, UVAS, Lahore, Pakistan

In this research work, pristine and various concentrations (2.4 wt%) of graphene oxide (GO)/carbon sphere (CS)–doped Al_2O_3 nanostructures (NSs) were synthesized with the chemical sol–gel method. Aluminum oxide (Al_2O_3) exhibits quick recombination of electrons and holes with a low specific surface to limit catalytic and antibacterial activities. Al_2O_3 doped with CS is good in wastewater treatment and reduces the size of NSs. The incorporation of graphene oxide (GO) into Al_2O_3 at different concentrations (2 and 4 wt%) enhances both the structural and chemical stabilities of the resulting material while concurrently decreasing the number of charge carriers and reducing the band gap energy. This modified Al_2O_3-GO composite exhibits promising potential for utilization in dye degradation and antibacterial activity. A series of characterizations were performed to investigate the structural, morphological, and optical properties. The NSs exhibited excellent catalytic activity (CA) against rhodamine B (RhB) dye in acidic, basic, and neutral media. The antimicrobial activity was tested against *Escherichia coli*. Pairs of electrons and holes are the primary building blocks for the production of reactive oxygen species (ROS), which causes bacteria to die. The significant inhibition zones against *E. coli* were calculated to be approximately 5.65 mm when compared to ciprofloxacin. Moreover, *in silico* investigations have revealed the possible inhibitory impact of produced nanomaterials (GO/CS-doped Al_2O_3) on DNA gyrase and FabI enzymes of fatty acid biosynthesis.

KEYWORDS

antimicrobial activities, dye degradation, molecular docking analysis, sol–gel method, carbon sphere, graphene oxide, aluminum oxide

1 Introduction

Water is a vital element for living things all around the world. Approximately 71% of the Earth's surface is covered with water, and hardly 0.03% is freshwater (Wang et al., 2018; Ikram et al., 2020a). Approximately 97.5% of water is salty, whereas the remaining 2.5% is usable, thus there is a scarcity of fresh water supply when compared to its high demand. Clean and safe consuming water shortage is one of the main issues in growing international places (Gadgil, 1998), therefore, around 750 million people are facing shortage of water (Ikram et al., 2021). Water contamination is a major global concern owing to industrial and radiological discharges containing heavy metals (cadmium, lead, mercury, and arsenic), synthetic organic dyes, and agricultural pesticides (Jamal et al., 2022). Synthetic dyes are drastically utilized in several industries such as polymers, textiles, cosmetics, paints, and pharmaceuticals (Ahmad et al., 2020). Organic dyes in contaminated water are the fundamental reason for increase in waterborne illnesses (World Health Organization, 2003). Aquatic creatures digest these toxic dyes. At the same time, these species are consumed by humans, which is pernicious to human health and subsequently increases micro-contaminants in waters that become unsafe for the ecosystem. A variety of dyes, which include rhodamine B (RhB), indigo red, black T (EBT), methylene blue (MB), and rose blue, are manufactured by industries and are known to contaminate freshwater resources (Rafiq et al., 2021). These dyes, specifically RhB (non-biodegradable organic-cationic textile dye), should be converted into less harmful forms through appropriate processes. Additionally, aquatic microbial pollution is a crucial issue due to the increase in world population, urbanization, and the lack of sanitary systems. Different microorganisms cause many diseases, such as diarrhea, typhoid, mastitis, and hepatitis; mainly, mastitis (by fungi, bacteria, and viruses) is a considerable burden for the dairy industry. Clinical malformations in the mammal glands and tissues of cattle and the physical and chemical variations in milk are all related to mastitis (Niu et al., 2017). Infectious bacteria, *Staphylococcus aureus* of the gram-positive type and *Escherichia coli* of the gram-negative kind have been associated with mastitis in livestock and are also known to cause diarrhea and nosocomial infections in human beings (Haider et al., 2020a; Baqir et al., 2021).

To eliminate hazardous dyes and pathogenic microorganisms from wastewaters, numerous techniques such as chemical precipitation, membrane filtration, electrochemistry, and ion exchange have been implemented to remediate contaminated water (Ikram et al., 2022a; Khan et al., 2022). The main issues with these methods are large-scale costs, immense energy consumption, and derived pollution from deficient dye removal and transfer (Bhattacharya et al., 2013). Adsorption is often used to break down reactive dye molecules during wastewater treatment (Deveci and Mercimek, 2019; Datta et al., 2021). Catalytic degradation is a suitable treatment for the degradation of dyes. Catalytic degradation with metal oxides is extremely power efficient, has the least virulence, and is environmentally friendly (Ali et al., 2019).

Nanotechnology plays a central part in the treatment of contaminated water. Nanomaterials-based inorganic semiconductors (ZnO, Bi_2O_3, CeO_2, La_2O_3, TiO_2, and Al_2O_3) have been extensively used as catalysts and bactericidal agents (Bhattacharya et al., 2013; Ikram et al., 2022b). Among these, Al_2O_3 has gained the attention of researchers in recent years attributed to its distinctive characteristics, which include greater surface area, mechanical strength, high hardness, and best chemical stability (Jiao et al., 2012). Al_2O_3 does not threaten the environment because it is chemically inert and does not undergo significant deterioration or transformation when exposed to environmental conditions. Under typical conditions of use, it is not anticipated to be harmful to the environment or human health. The precise manufacturing processes that are used have a direct bearing on the environmental impact of Al_2O_3 synthesis. Efforts are currently being made to reduce the environmental footprint of Al_2O_3 synthesis by employing more sustainable and friendlier methods (Jaishankar et al., 2014). The use of CS/GO in applications has positive effects on the environment, such as increasing the efficacy of wastewater treatment and decreasing the requirement for toxic chemicals (Holder et al., 2017). Moreover, it has appreciable applications in optical lenses, anticorrosive films, humidity sensors and electronic devices, and petrochemical industries (Jirátová and Beránek, 1982; Asada et al., 2008). Various phases of Al_2O_3 have band gap energy from 3.2 to 4.3 eV (Costina and Franchy, 2001). This considerable band gap energy restricts antimicrobial activity and dye degradation (Said et al., 2016).

The non-metals carbon, nitrogen, and sulfur have been found to decrease the band gap energy of metal oxides by doping (Ahn et al., 2008). Carbon spheres (CSs) have been utilized as a dopant material with remarkable adsorption properties, boasting a specific surface area of 207 m^2/g (Ge et al., 2015). It has been demonstrated that the inclusion of carbon spheres (CSs) in nanomaterials increases their adsorption capacity, induces a redshift in their band gap energy, promotes good dispersion, and exhibits biocompatibility. CSs perform well in drug delivery systems, catalytic activities, antibacterial activities, and cellular labeling (Ge et al., 2015). Using carbon-based materials to formulate active catalysts enhances the antibacterial and catalytic activities of NSs and extends the lifetime of photo-generated electron–hole pairs. The graphene chemical derivative known as graphene oxide (GO) is a two-dimensional (2D) atomic sheet composed of sp^2 carbon atoms, which possesses distinctive mechanical properties and exceptional catalytic performance (Bu et al., 2013). Thick sheets of GO have been widely considered for different applications (Amirov et al., 2017). Notably, GO exhibits high electron mobility and a wide surface area that reaches approximately 736.6 m^2/g in theoretical terms (Montes-Navajas et al., 2013). In addition, GO demonstrates robust chemical stability while possessing numerous active sites and a high absorption activity (Yilmaz et al., 2022). GO is an excellent option for Al_2O_3-based catalysts because of the surface functionality of hydroxyl/carboxyl groups, and its ability for charge-separation properties results in excellent hydrophilicity and negative charge (Sharma et al., 2020). GO has desirable catalytic properties to improve CA and can eliminate organic dyes through the adsorption phenomenon due to its more excellent adsorption surface (Gordani et al., 2022).

This work aimed to study the impact of a fixed CS concentration and varied GO concentrations (2 and 4 wt%) on Al_2O_3 NSs

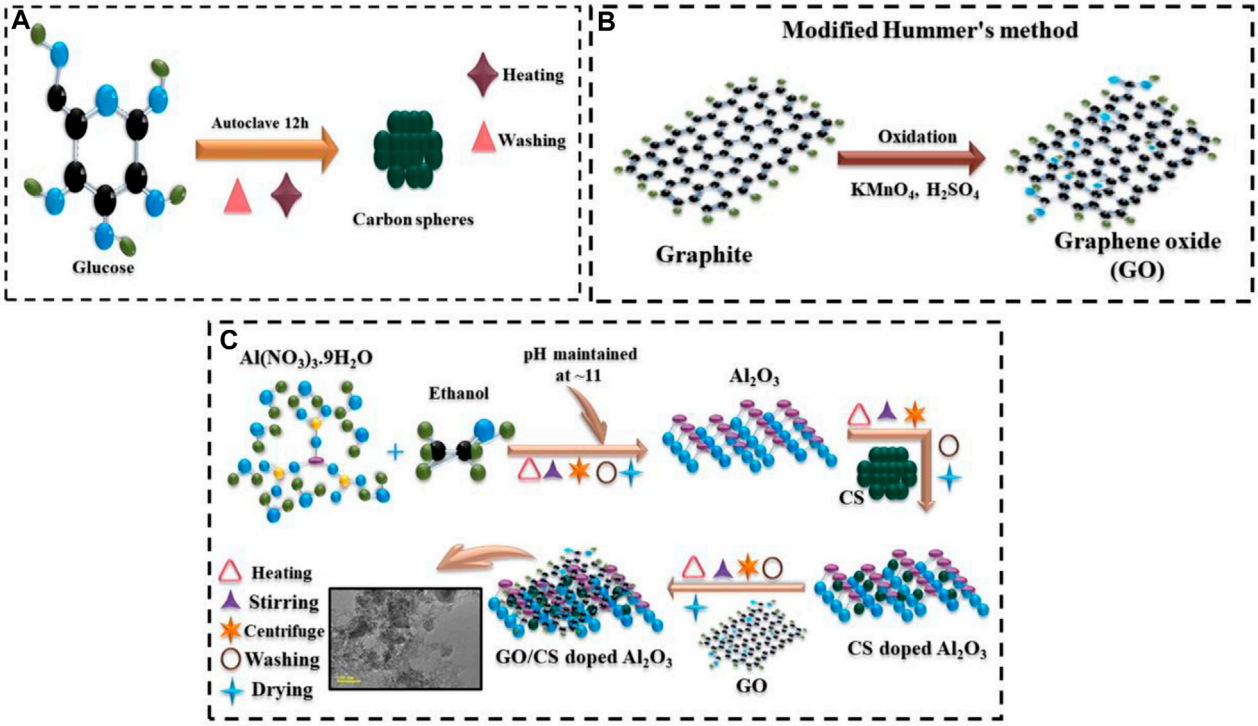

FIGURE 1
Schematic illustration of the synthesis of **(A)** carbon sphere, **(B)** graphene oxide, and **(C)** (2 and 4 wt%) GO/CS-Al_2O_3.

synthesized by the sol–gel method. The effect of GO/CS-doped Al_2O_3 was examined by studying its catalytic degradation behavior, antimicrobial activity, and molecular docking analysis with various characterizations to study its optical, morphological, and structural properties.

2 Experimental section

2.1 Materials

The chemical reagents employed in the experiment are aluminum nitrate nonahydrate ($Al(NO_3)_3$ $9H_2O$; 97%, DUKSAN), sodium hydroxide (NaOH; 99%, Sigma-Aldrich), glucose ($C_6H_{12}O_6$, Sigma-Aldrich), ethanol (C_2H_5OH; >99.8%, Sigma-Aldrich), hydrochloric acid (HCl; 37%, Sigma-Aldrich), graphite powder (99.5%, BDH Laboratory Supplies), potassium permanganate ($KMnO_4$; 99.5%, AnalaR), sulfuric acid (H_2SO_4; 97%, AnalaR), hydrogen peroxide (H_2O_2; 50%, AnalaR), and deionized water (DI-H_2O). All reagents have been used directly without any purification.

2.2 Synthesis of CS

The hydrothermal carbonization method was applied for CS synthesis. Glucose solution (1 M) was kept in the autoclave for 12 h at 180°C. Precipitates were found, washed with DI-H_2O, and dried for 12 h at 100°C.

2.3 Synthesis of pure and GO/CS-doped Al_2O_3

The sol–gel method was employed to obtain GO/CS-doped Al_2O_3 NSs, and 0.5 M (6.25 g/33 mL) of $Al(NO_3)_3$ $9H_2O$ was used to prepare NSs by constant stirring at 80°C. Furthermore, a fixed amount of ethanol was incorporated into the above solution. After 20 min, 1 M NaOH was introduced drop by drop to obtain precipitates until the pH ~11 was maintained. The precipitated solution was stirred for 2 h and washed with deionized water using centrifugation at 7,000 rpm for 7 min twice. Finally, the pure product was dried at 120°C overnight and ground to obtain fine powders. GO was synthesized by the modified Hummer's method in the laboratory (Ikram et al., 2020b). The process utilized in this study involved synthesizing a constant quantity of CS (187 mg) along with varying concentrations [2 wt% (125 mg) and 4 wt% (250 mg)] of GO-doped Al_2O_3 nanomaterials.

2.4 Catalytic activity

Catalytic activity (CA) of pristine and (2 and 4 wt%) GO/CS-Al_2O_3 was carried out against RhB dye. All reagents, which included RhB and $NaBH_4$, were freshly prepared to ensure the purity of the experimental results. 10 mg/L of RhB solution was divided into three equal parts to maintain the pH for basic, neutral, and acidic mediums (Ullah et al., 2021). Together, 3 mL of the dye and 400 µL of $NaBH_4$ were combined, and 400 µL of synthesized materials (acting as catalysts) were incorporated to check the

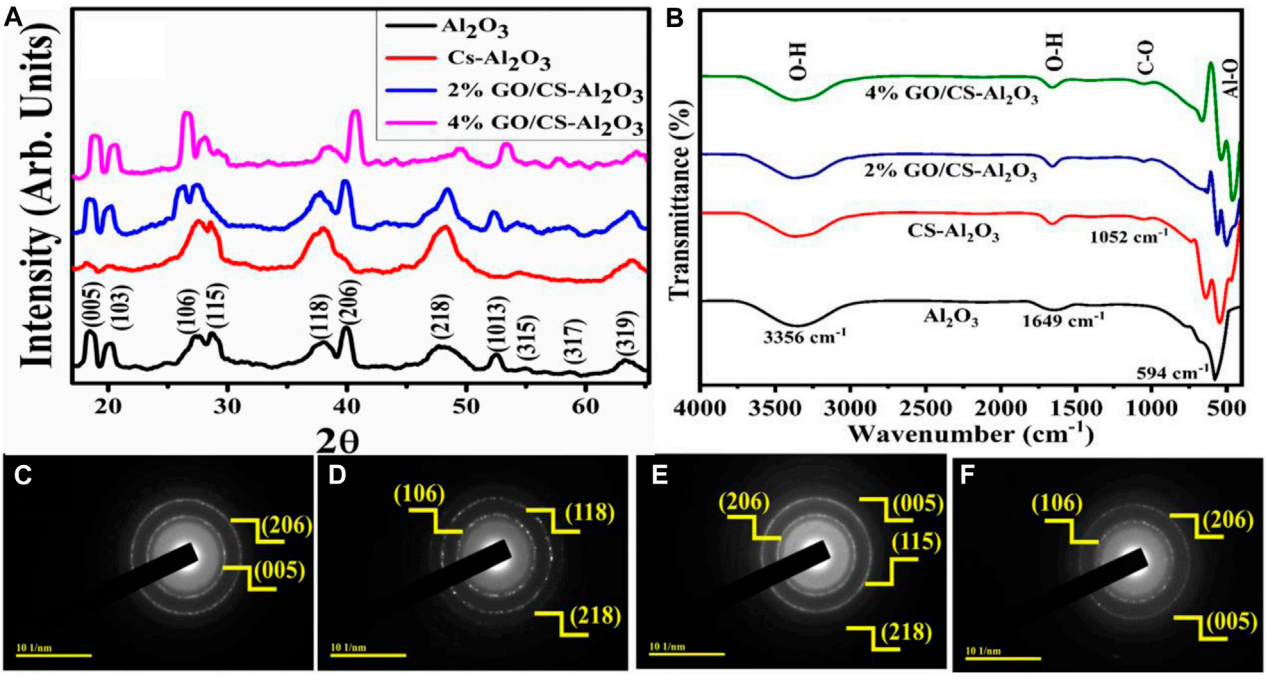

FIGURE 2
(A) X-ray diffraction spectra before degradation of dye, **(B)** FTIR spectra, and **(C–F)** SAED images of GO/CS-doped Al_2O_3 NSs.

degradation. A catalyst was employed to minimize the surface activation energy of the reaction, which increases reaction stability and efficiency. The absorption variation spectra were spectrophotometrically acquired using a UV-vis spectrophotometer at regular intervals. RhB shows its absorption signal at 554 nm (Vijayan et al., 2019). Reduction of RhB occurred, resulting in a color change from pink to colorless. The percentage degradation was calculated using the following formula

$$\% \text{ degradation} = (C_o - C_t)/C_o \times 100,$$

where C_o is the initial absorbance and C_t is the final absorbance at a specific time after the incorporation of materials.

2.5 Isolation and identification of MDR *E. coli*

2.5.1 Sample collection and isolation

Direct milking into sterile glassware was used to collect raw milk samples from lactating cows marketed at various markets, veterinary hospitals, and farms in Punjab and Pakistan. The raw milk was promptly transported to the laboratory at a temperature of 4°C. To enumerate the coliform bacteria in the raw milk, MacConkey agar was utilized, and all plates were incubated at 37°C for 48 h.

2.5.2 Identification and characterization of bacterial isolates

Based on colonial morphology, Gram stain, and several biochemical tests, the initial identification of *E. coli* was made using the Bergey's Manual of Determinative Bacteriology, as shown in Supplementary Figure S1 (Sinclair, 1939).

2.5.2.1 Antibiotic susceptibility

Mueller–Hinton agar (MHA) was used to conduct the antibiotic susceptibility test using the disk diffusion method (Bauer et al., 1966). The test was carried out to ascertain whether *E. coli* was resistant to the following antibiotics (classes): gentamicin (CN) 10 µg (aminoglycosides), ceftriaxone (CRO) 30 µg (cephalosporins), amoxycillin (AX) 25 µg (penicillin), imipenem (IPM) 10 µg (carbapenem), tetracycline (TE) 30 µg (tetracyclines), azithromycin (AZM) 15 µg (macrolides), ciprofloxacin (CIP) 5 µg (quinolones), Septran (SXT) 25 µg, and Augmentin (AMC) 30 µg (Feuerstein et al., 2022). *E. coli* purified cultures were developed and brought to 0.5 MacFarland turbidity. They were spread-plated on MHA (Oxoid Limited, Basingstoke, United Kingdom), and the antibiotic disks were positioned far enough away from each other on the inoculated plate's surface to prevent the overlying of inhibition zones. The Clinical and Laboratory Standard Institute (NCCLS, 2007) was used to evaluate the results after 24 h at 37°C incubation on plates as presented in Supplementary Figure S2 and Supplementary Table S1. Multidrug resistant (MDR) was assigned to bacteria that tested positive for resistance to at least three drugs (Iwalokun et al., 2004).

2.5.2.2 Antimicrobial activity

Using the agar well diffusion method on 10 characteristic isolates of MDR *E. coli* obtained from mastitis milk, the *in vitro* antibacterial action potential of pristine and (2 and 4 wt%) GO/CS-doped Al_2O_3 nanoparticles was assessed. On MacConkey agar, 1.5×10^8 CFU/mL (0.5 McFarland standard) MDR *E. coli* were swabbed onto Petri dishes. A sterile cork borer was used to create 6 mm wide wells. Various concentrations of pure and (2.4%) GO/CS-doped

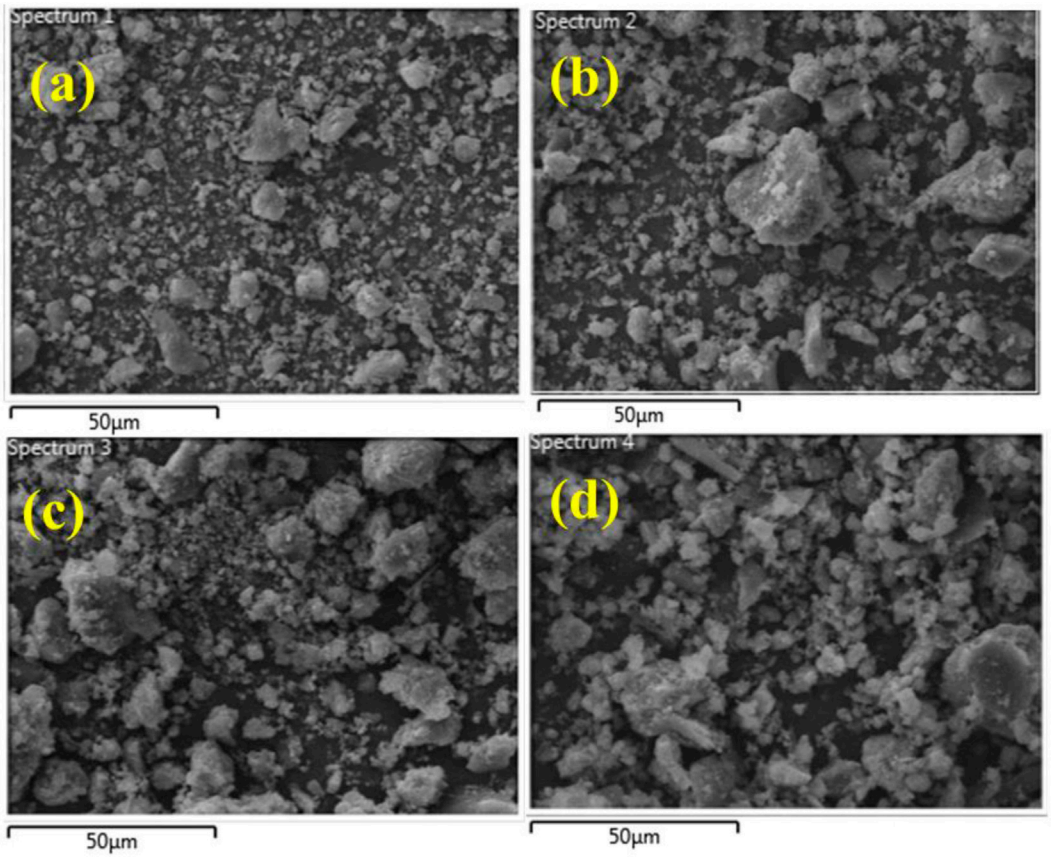

FIGURE 3
FE-SEM images of **(A)** Al_2O_3, **(B)** CS-doped Al_2O_3, **(C)** 2% GO/CS-doped Al_2O_3 NSs, and **(D)** 4% GO/CS-doped Al_2O_3 NSs.

Al_2O_3 were used, such as 0.5 mg/50 µL and 1.0 mg/50 µL. The positive control was ciprofloxacin (0.005 mg/50 µL) (Naika et al., 2015), while the negative control was DI-H_2O (50 µL) (Haider et al., 2020b).

2.5.2.3 Statistical analysis

The inhibition zone (millimeters) was used to measure the antimicrobial efficiency with one-way analysis of variance (ANOVA) in SPSS 20 (Haider et al., 2020a), diameters of the inhibition zones were examined, and results were declared statistically significant at $p < 0.05$.

2.6 Molecular docking analysis

Molecular docking on DNA gyrase and enoyl-[acyl-carrier-protein] reductase (FabI) from *E. coli* were the objectives concerning the nucleic acid and fatty acid biosynthesis pathways, respectively, with PDB identifier (PDB ID: 5MMN; resolution: 1.90 Å) (Panchaud et al., 2017; Ikram et al., 2022c) and FabI (PDB ID: 1MFP; resolution: 2.33) (Seefeld et al., 2003). Three-dimensional (3D) structures were downloaded from the Protein Data Bank using the matching PDB IDs. The sybyl X-2.0 software (Altaf et al., 2020; Mehmood et al., 2022) was used to predict molecular docking via sketch module–built ligand structures. The water molecules containing their natural ligands were removed, polar H-atoms were added to the molecule, and energy was preserved. PyMOL was used to create a 3D depiction of binding interactions.

3 Results and discussion

The hydrothermal carbonization method applied for CS synthesis is represented in Figure 1A. GO synthesized by the modified Hummer's approach in the laboratory is depicted in Figure 1B. The sol–gel method used to synthesize the pristine and (2.4%) GO/CS-doped Al_2O_3 is represented in Figure 1C.

The phase composition, crystallinity, crystal structure, and crystalline size of the synthesized pristine and (2 and 4 wt%) GO/CS-doped Al_2O_3 NSs have been investigated using XRD analysis. The XRD patterns indicated the diffraction angle in the range of $2\theta = 15^{\circ}$–65° and are shown in Figure 2A. Al_2O_3 exhibits the diffraction peaks at 18.7°, 19.4°, 27.6°,29.3°, 37.9°, 39.4°, 47.5°, 52.8°, 55.3°, 58.8°, and 63.2° corresponding to crystal planes (005), (103), (106), (115), (118), (206), (218), (1013), (315), (317), and (319), respectively. The peaks obtained indicate that the structure of $Al_{2\cdot67}O_4$ is a tetragonal one and belongs to the space group P-4m2, and the space group number 119 matched up with the JCPDS card number 01-088-1609, the mentioned peaks are also matched

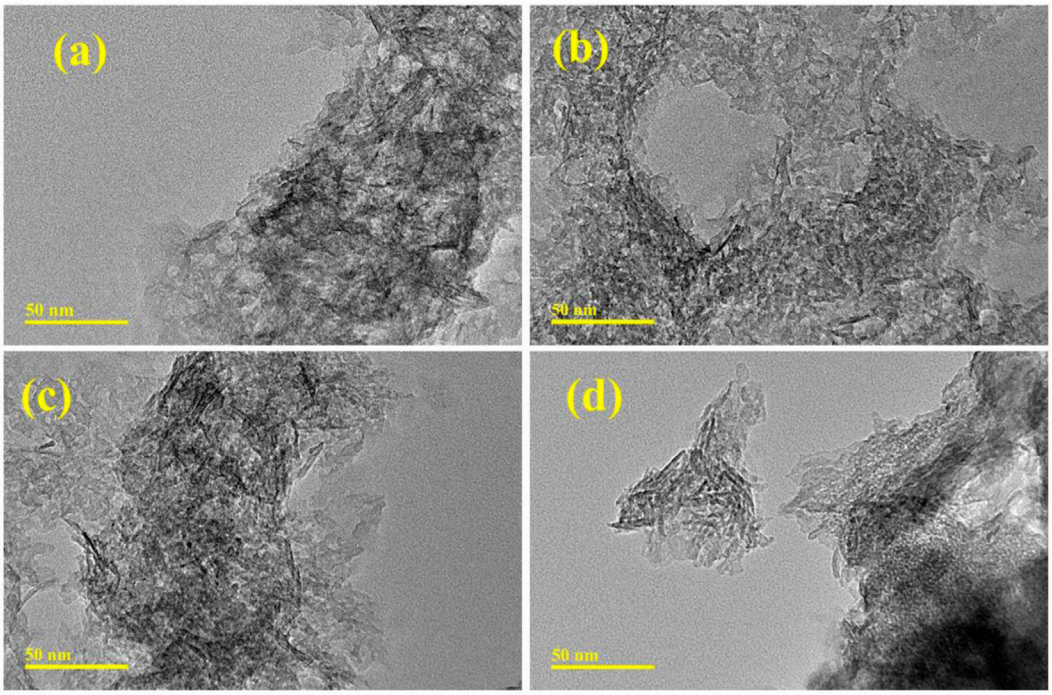

FIGURE 4
TEM images of **(A)** Al_2O_3, **(B)** CS-doped Al_2O_3, **(C)** 2% GO/CS-doped Al_2O_3 NSs, and **(D)** 4% GO/CS-doped Al_2O_3 NSs.

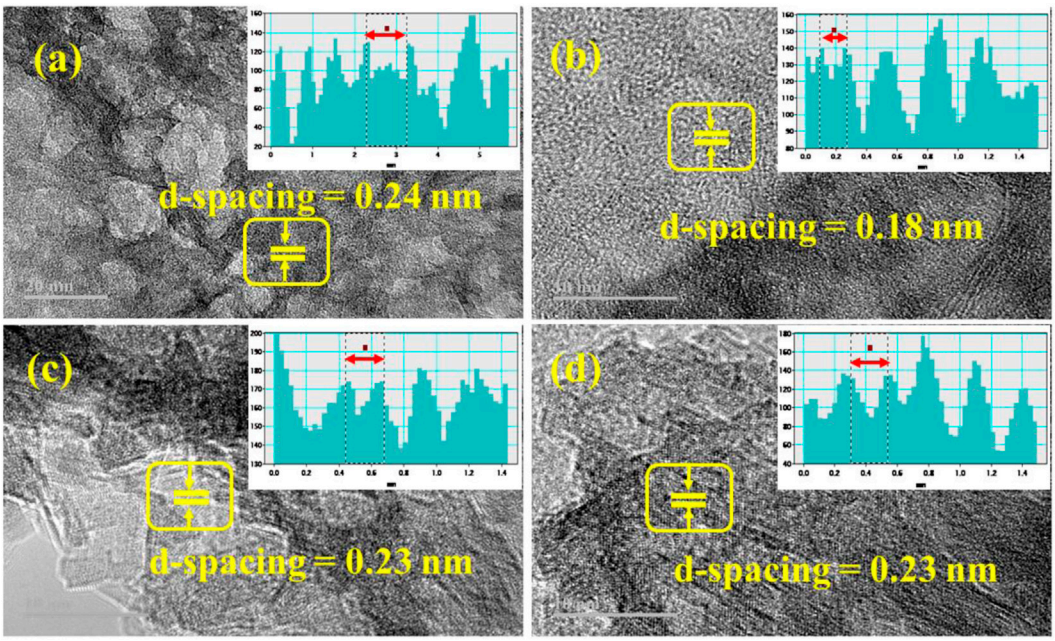

FIGURE 5
HR-TEM images of **(A)** Al_2O_3, **(B)** CS-doped Al_2O_3, **(C)** 2% GO/CS-doped Al_2O_3 NSs, and **(D)** 4% GO/CS-doped Al_2O_3 NSs.

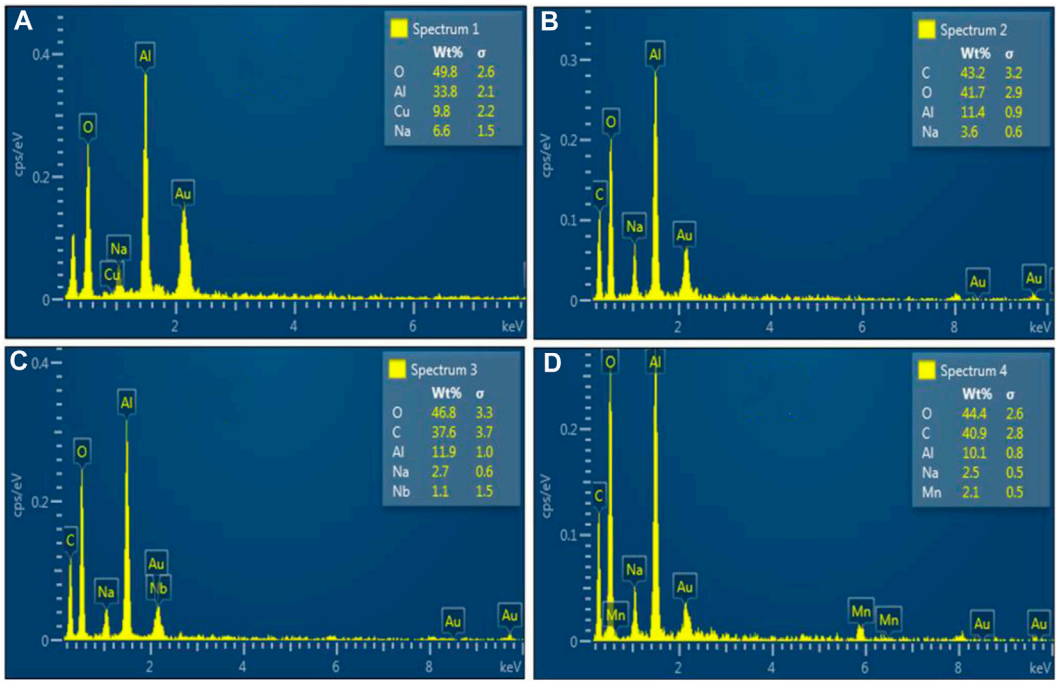

FIGURE 6
EDS analysis of **(A)** Al_2O_3, **(B)** CS-doped Al_2O_3, **(C)** 2% GO/CS-doped Al_2O_3 NSs, and **(D)** 4% GO/CS-doped Al_2O_3 NSs.

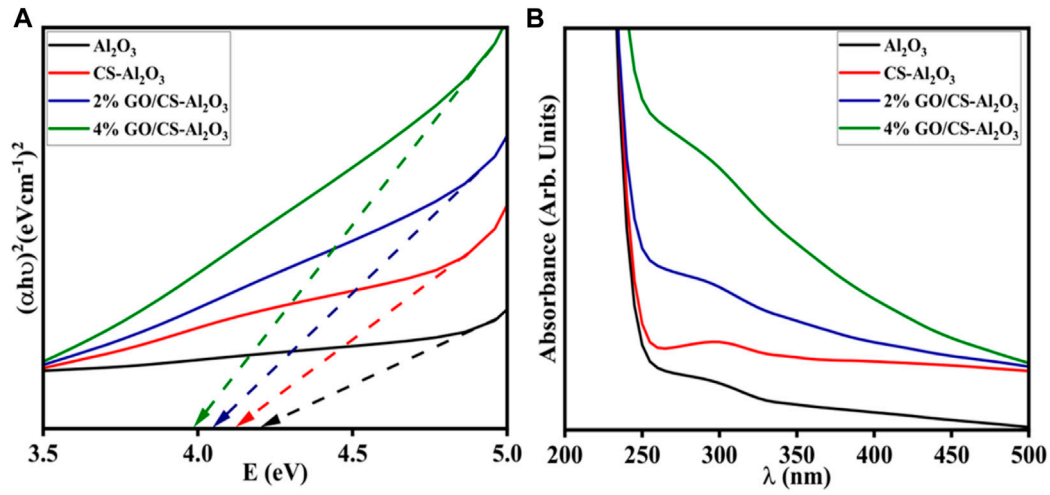

FIGURE 7
(A) UV-vis absorption spectra and **(B)** energy band gap calculation.

with the JCPDS card number 00-031-0026 of Al_2O_3. With the incorporation of GO/CS, the peak intensity slightly increased, and the full width at half maxima decreased, which increased the crystallinity and crystalline size of the synthesized sample indicated in the XRD analysis spectra. The crystallite size (D) of the synthesized NSs has been calculated through the Debye–Scherrer's formula $D = 0.89\lambda/\beta\cos\theta$. The measured value of crystallite sizes are 17.6, 24.8, 15.7, and 14.7 nm with corresponding (206), (118), (206), and (206) planes for pristine and GO/CS-doped Al_2O_3, respectively. The diffraction angles and effect of peak broadening substantially influenced the crystalline size. The practical consequences show that the crystalline size increases with CS incorporation and reduces with increasing GO/CS concentrations (2 and 4 wt%).

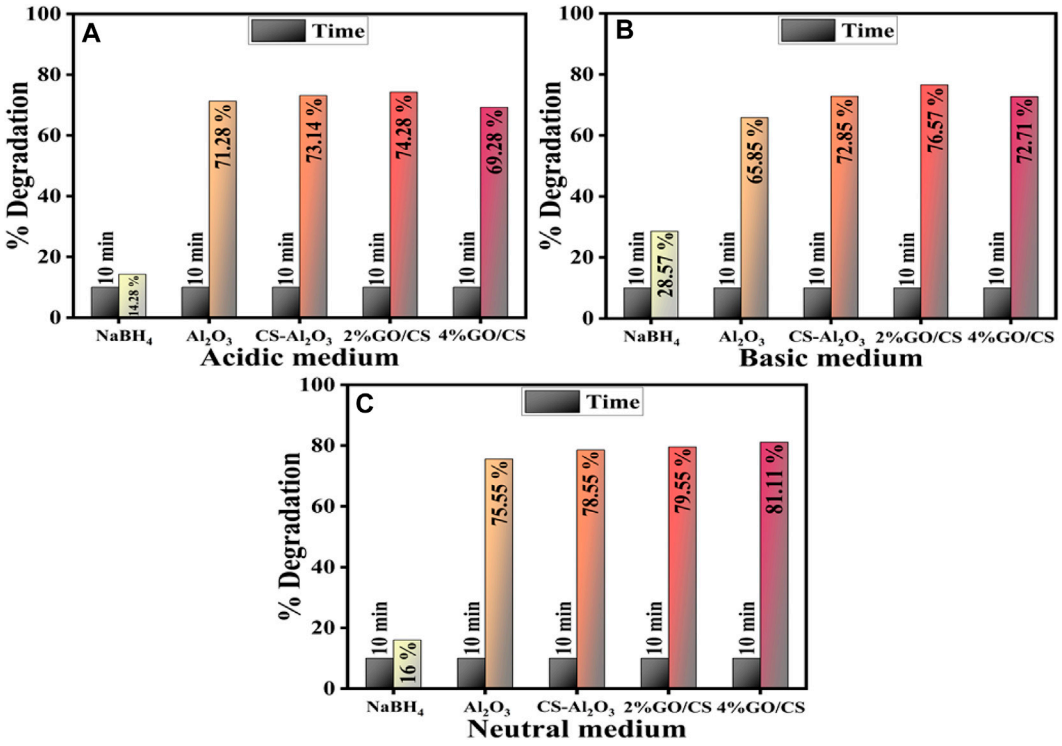

FIGURE 8
Catalytic activity of pure and (2 and 4 wt%) GO/CS-doped Al_2O_3 NSs in **(A)** acidic medium **(B)** basic medium, and **(C)** neutral medium.

The FTIR analysis was employed to investigate the chemical structure of pristine and GO/CS-doped Al_2O_3 NSs and the existence of the different functional groups in the 4,000–400 cm^{-1} region that is represented in Figure 2B. The band that appeared between 700 and 500 cm^{-1} is associated with Al-O-Al and Al-O vibrations, the intensity increased upon doping, and the peaks shifted to a lower wavenumber (Atrak et al., 2018; Mahmoud et al., 2022). The broadband observed at approximately 3,356 cm^{-1} and the weak band at 1,649 cm^{-1} were attributed to the stretching vibrations of the O-H group. These spectral features indicate that the material was exposed to a damp atmosphere, which had resulted in the development of the observed O-H vibrations (Gao et al., 2017; Moeen et al., 2022). On CS/GO doping, the band appeared at 1,052 cm^{-1} assigned to C-O vibration, demonstrating the doping effect and indicating the collaboration of the doped material (Cintrón and Hinchliffe, 2015).

The use of selected area electron diffraction (SAED) analysis has facilitated the identification of the crystalline nature of the synthesized materials and their classification as a single, polycrystalline, or semi-crystalline crystal. The synthesized samples indicate bright circular rings of Al_2O_3 and (2 and 4 wt%) GO/CS-doped Al_2O_3 NSs that are polycrystalline, as shown in Figures 2C–F. The indexed rings are in good agreement with the findings of the XRD analysis, which strongly indicates that the products were developed of an exceptionally crystalline nature.

The surface morphology of the synthesized pristine GO/CS-doped Al_2O_3 NSs was identified using the FE-SEM analysis which is shown in Figures 3A–D. The pristine sample shows the aggregation of Al_2O_3 nanoparticles and the CS-doped Al_2O_3 specimen shows the increase in the size of the particle and also the agglomeration of nanoparticles. With the incorporation of GO at low and high concentrations, the aggregation and agglomeration increased which show that the nanoparticles are linked with each other. The agglomerated nanoparticles are further explained in the TEM morphological images that indicate the rod- and wire-like morphologies.

The TEM analysis was utilized to indicate the topography and morphological information of pristine and (2 and 4 wt%) GO/CS-doped Al_2O_3 NSs as displayed in Figures 4A–D. Al_2O_3 exhibits the agglomeration and aggregation of nanowires (NWs). Upon CS doping, the agglomeration decreased the overlapping of nanorod (NR)- and NW-like morphological structures. With the low concentration of GO doping, the nanowires were generated as shown in Figure 4C. At a high concentration of 4% GO, the rod-like structure of the material was observed to be covered with a sheet, leading to an increase in agglomeration. Consequently, the level of crystallinity was reduced.

The interlayer distance between the lattice fringes of the prepared NSs in the HR-TEM micrograph is calculated using the Gatan software, as shown in Figures 5A–D. The measured d-spacing value of pristine Al_2O_3 is 0.24 nm, corresponding to the (206) plane. The CS-doped Al_2O_3 has a d-spacing value of 0.18 nm corresponding to the plane (218). The (2.4 wt%) GO/CS-doped Al_2O_3 NSs have a d-spacing value of 0.23 nm related to the plane (206). The interlayer d-spacing closely matches the XRD

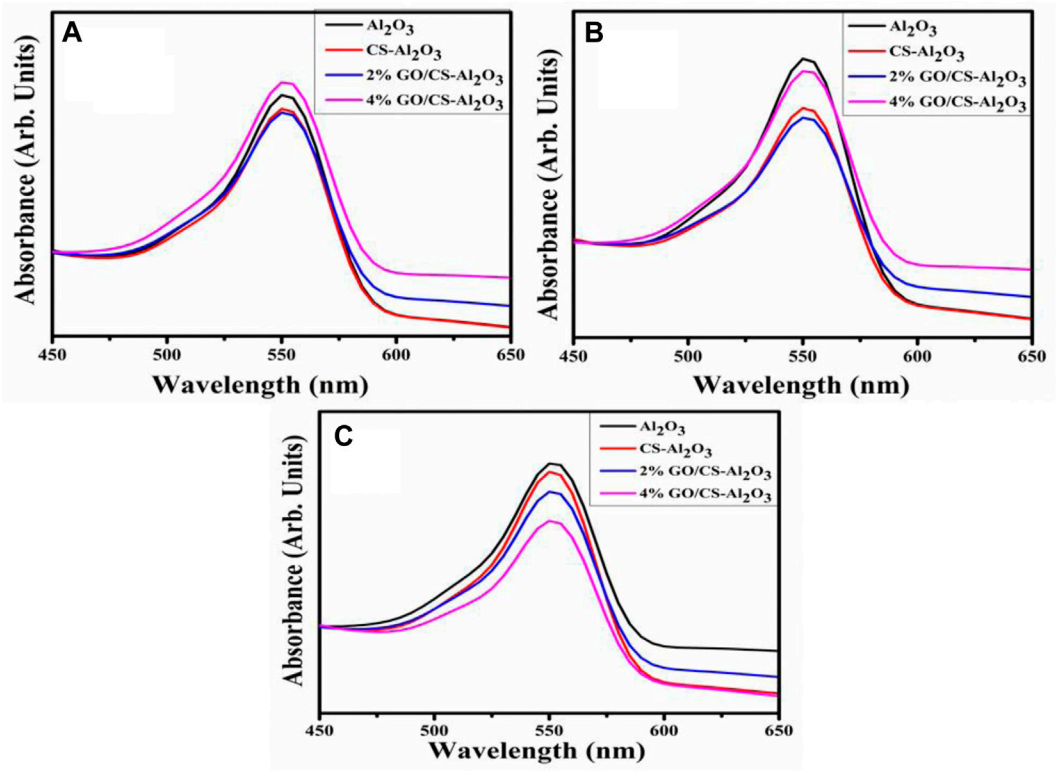

FIGURE 9
UV-vis spectra of dye reduction: **(A)** acidic medium, **(B)** neutral medium, **(C)** basic medium.

measurement and is compatible with JCPDS card number 01-088-1609.

The chemical composition of the synthesized NSs was identified using the EDS analysis and shows the elemental composition of synthesized material with atomic percentages of elements (Figures 6A–D). EDS represents Al_2O_3 constituents Al and O peaks, while C peaks confirm the presence of doped (CS/GO) materials. The Na peaks appeared due to the incorporation of NaOH to maintain the pH during synthesis (Ikram et al., 2022d). The samples had a gold coating to them such that there would be no surface charge but help with secondary electron emission. In research laboratories, gold is the ideal conductive metal for coating, acts as a superb conductor, and does not rust (Bilal et al., 2022). The Cu tape in the sample holder is responsible for the appearance of the Cu peak (Shujah et al., 2022). However, the sample preparation and experimental design were responsible for the appearance of the manganese (Mn) and niobium (Nb) peaks.

Ultra-visible absorption spectroscopy has been used over the wavelength range of 200–500 nm to evaluate the optical absorption properties and band gap of the synthesized pristine and (2 and 4 wt%) GO/CS-doped Al_2O_3, as shown in Figure 7A. The λ_{max} of the undoped and doped NSs are observed in the 285–300 nm range due to π-π* and n-π* transition by various functional groups (such as >C=O, -OH, etc.) present in the material (Penner, 2017), while the λ_{max} of Al_2O_3 was approximately 288 nm as reported in a previous work (Yuan et al., 2015). By applying the Tauc's plot equation, the direct band gap of pure Al_2O_3 was observed at 4.2 eV (Omanwar et al., 2018), as shown in Figure 7B. The doping of CS and (2 and 4 wt%) GO/CS band gap energy decreased 4.1, 4.0, and 3.9 eV due to the redshift in the wavelength by the Brustein–Moss effect (Zhu et al., 2016). A decrease in the band gap may be attributed to increased crystallized size upon doping (Ikram et al., 2022d).

The catalytic activity is significantly dependent upon the crystallite size, surface area, and morphology of the catalyst (Ikram et al., 2022d), along with the pH and temperature of the dye solution that have a significant impact on the CA of the catalyst (Tju et al., 2017). Using a UV-vis spectrophotometer, the catalytic activities of pure and doped Al_2O_3 were investigated. The lysis of RhB seems negligible in all mediums with $NaBH_4$ while the undoped, CS, and (2.4%) GO/CS-doped Al_2O_3 NSs showed maximum degradation in neutral medium (75.5%, 78.55%, 79.55%, and 81.11%), respectively, at a pH of ~7. In a basic medium with a pH of ~12, the CA was observed to be higher (65.85%, 72.85%, 76.57%, and 72.71%) than it was in an acidic medium (71.28%, 73.14%, 74.28%, and 69.28%). This trend is depicted in Figures 8A–C, which is attributed to the presence of hydroxyl (OH) groups generated by the addition of NaOH (Vijayan et al., 2019). Additionally, the cationic nature of RhB further favors a basic medium, as the electrostatic attraction between the positively charged surface of the catalyst and RhB molecules increases (Javaid and Qazi, 2019). By changing the pH of the solution, the dye degradation efficiency was altered due to the enhancement of repelling electrostatic forces between RhB and H^+ ions produced

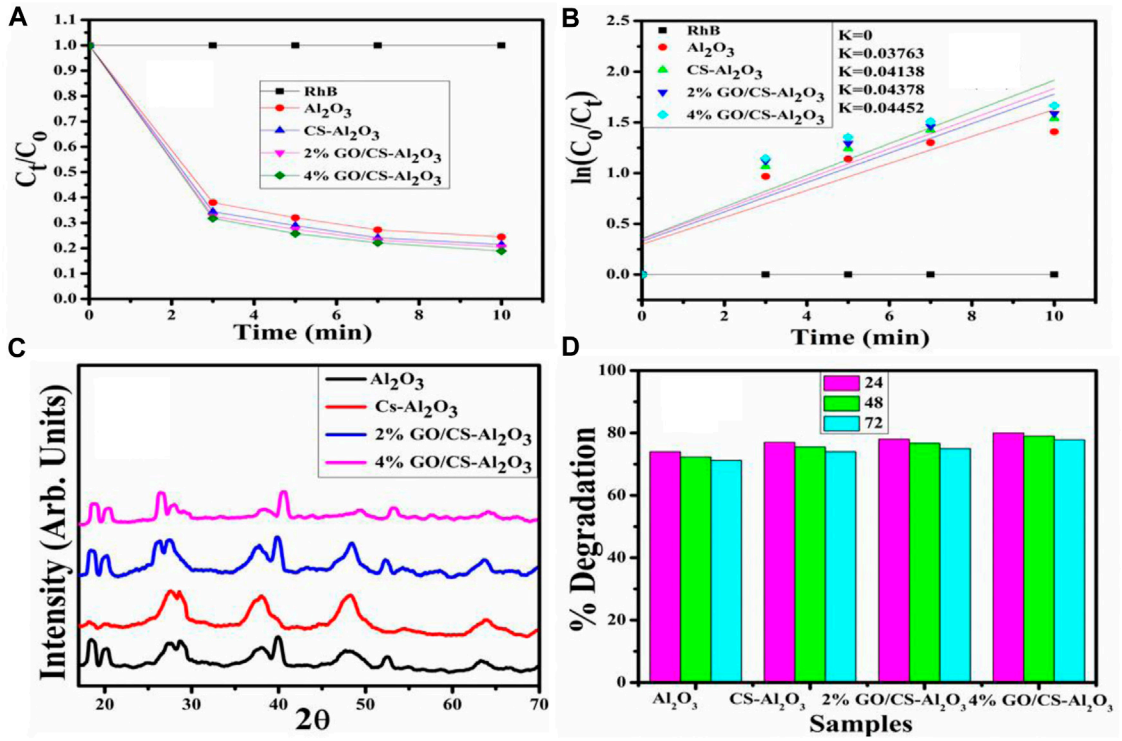

FIGURE 10
(A) Plot of the concentration ratio (C_t/C_0) vs. time, **(B)** plot of ln (C_0/C_t) vs. time spectra for dye reduction, **(C)** X-ray diffraction spectra after degradation of dye, and **(D)** reusability of the catalyst in the neutral medium.

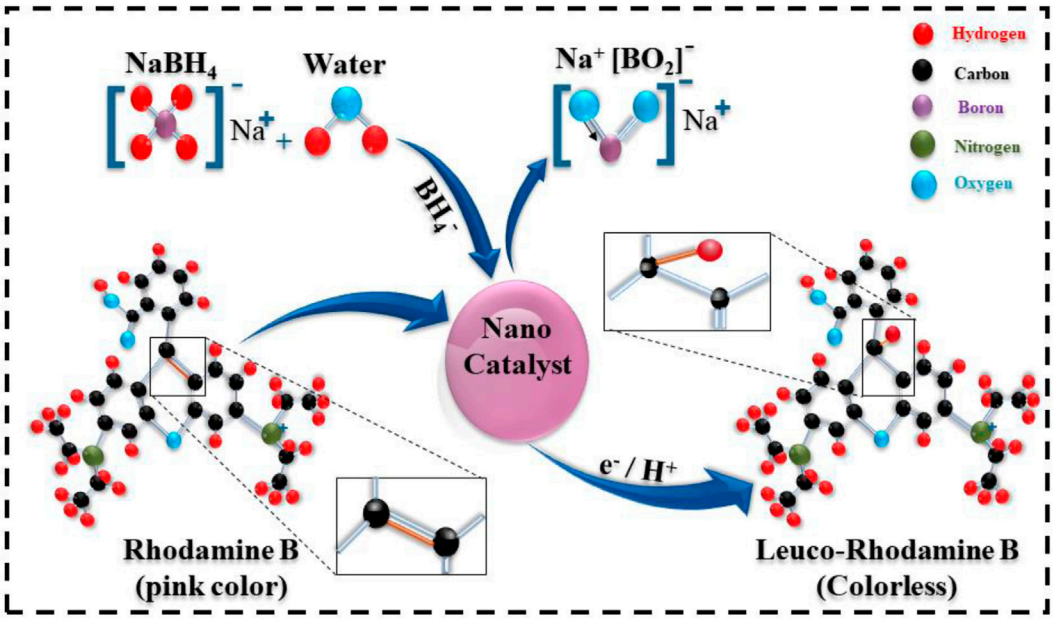

FIGURE 11
Schematic description of catalytic performance.

TABLE 1 Inhibition zone at low and high concentrations for *E. coli*.

Samples	Inhibition zones (mm)	
	0.5 mg/50 µL	1.0 mg/50 µL
Al_2O_3	2.75 ± 0.04	3.95 ± 0.03
CS-Al_2O_3	3.30 ± 0.03	4.15 ± 0.02
2% GO	4.25 ± 0.03	4.70 ± 0.03
4% GO	4.70 ± 0.02	5.65 ± 0.02
Ciprofloxacin	9.55 ± 0.01	9.55 ± 0.01
DI-H_2O	0 ± 0.0	0 ± 0.0

from the acidic solution; the CA of the acidic solution was reduced (Javaid and Qazi, 2019).

It has been demonstrated that the synthesized NSs can catalytically degrade the dye through the transfer of electrons from $NaBH_4$ to the dye molecule. Using UV-vis spectroscopy, the catalytic reduction of RhB by incorporating the reducing agent $NaBH_4$ influenced the degradation when using NSs. The degradation of RhB dye was monitored and the consequences are shown in Figures 9A–C.

The incorporation of 2% GO/CS-Al_2O_3 resulted in an increased percentage of degradation in all media, as there was an increase in the number of active sites in the catalyst lattice. However, in the case of 4% GO/CS-Al_2O_3, the increase in active sites was observed only in acidic and basic media. This is likely due to the agglomeration of the nanomaterial caused by the higher GO content in the catalyst, which may have resulted in a shielding effect that affected the active sites. Additionally, it is possible that a reaction occurred between H^+ and OH^- ions in acidic and basic media, respectively, and the surface of GO contains oxygenated functional groups such as COOH and OH, resulting in the deformation of its structure (Javaid and Qazi, 2019).

The increased catalytic activity can be attributed to the large surface area of the GO/CS-doped Al_2O_3 NSs. As a consequence of this, the catalytic degradation of RhB by 4 wt% GO/CS-doped Al_2O_3 NSs was significantly improved, and the dye was degraded efficiently. The plot of C_t/C_0 vs. time for RhB degradation reveals that the dye continuously degraded with the increase of time over NSs, indicating the rapid degradation of the RhB dye (Rahman et al., 2013; Rahman et al., 2017). The catalytic degradation kinetics has the rate constant (k) calculated by determining the slopes of the $\ln(C_0/C_t)$ function against the passage of time as indicated in Figures 10A, B. The calculated values for the degradation rate constant k for pristine and doped NSs are 0.03763, 0.04138, 0.04378, and 0.04452 min^{-1}. In addition, the stability of 4% GO/CS-doped Al_2O_3 was investigated using XRD that indicated the XRD pattern of the synthesized sample after degradation of the RhB dye exhibited that the peak intensity decreased so that crystallinity decreased, which is shown in Figure 10C. The prepared samples are stable up to a maximum of three cycles, as shown in Figure 10D. After the third cycle, there was a reduction in crystallinity of the QDs as a result of the dissolution and corrosion of the catalyst.

The catalytic mechanism is shown in Figure 11, in which the reducing agent and nanocatalyst are prime factors essential for the degradation of the RhB dye. The CA redox reaction involved the e^- transfer from the reductant to the oxidant. As a result, the breakdown of the dye occurred by electron absorption. In the presence of $NaBH_4$, the reaction was prolonged and less effective. Nanocatalysts (Al_2O_3 and (2.4 wt%) GO/CS-doped Al_2O_3) were incorporated into oxidation–reduction reactions to overcome these issues. $NaBH_4$ acted as the reducing agent for the degradation of RhB (which acts as the oxidizing agent by receiving e^-), and the catalyst acts as an electron relay by transferring electrons from $NaBH_4$ to RhB. NSs increased the adsorption of BH_4^- ions along with dye molecules through many active sites, resulting in quicker and more efficient degradation of the dye (Ikram et al., 2021; Bari et al., 2022). Reducing agents

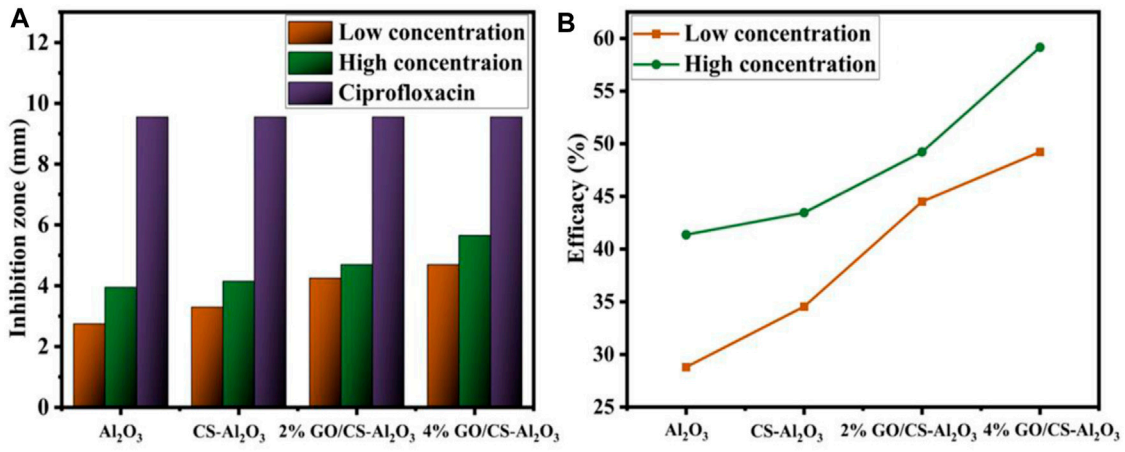

FIGURE 12
Graphical representation of inhibition zones: **(A)** comparative study of inhibition zones and **(B)** % age efficiency of pristine and GO/CS-doped Al_2O_3 for *E. coli*.

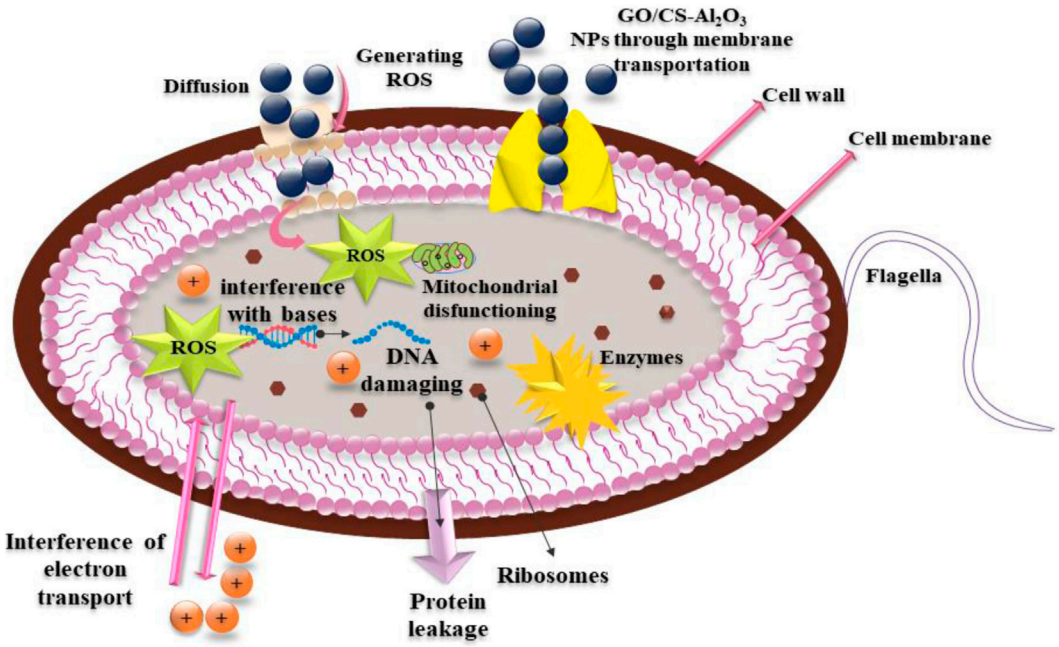

FIGURE 13
Schematic diagram of antibacterial mechanism.

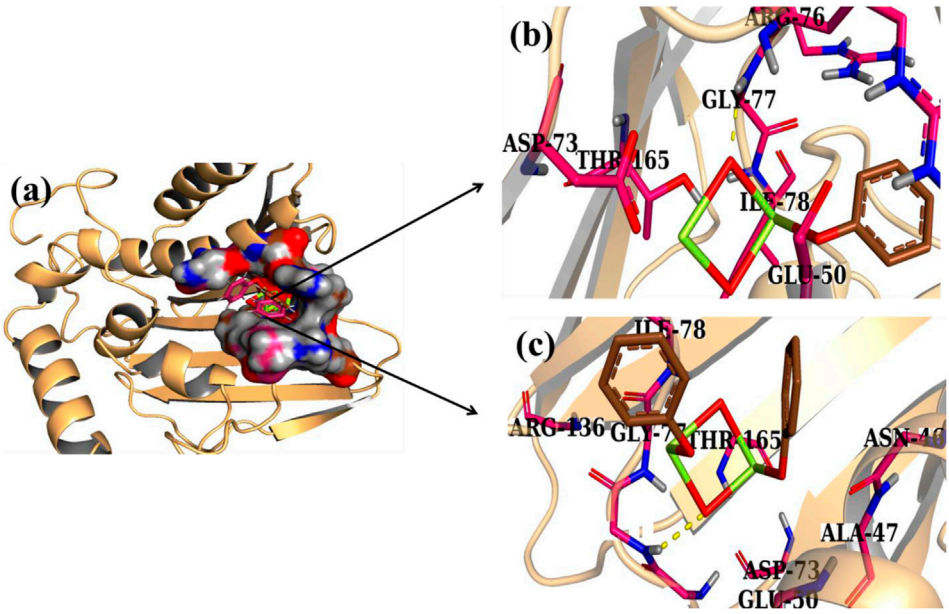

FIGURE 14
3D view of binding interaction of nanocomposites within the active site of DNA gyrase$_{E.coli}$, **(A)**, CS-doped Al_2O_3 **(B)**, and GO/CS-doped Al_2O_3 **(C)**.

together with the nanocatalyst's presence increases the degradation percentage.

The catalyst's small size and greater surface area provide more active sites, enhancing the catalytic activity. Microporosity blocks the active sites if the catalyst has a large surface area and degradation efficiency diminishes. The reaction is slow without a catalyst, and incorporating a catalyst increases the degradation of the dye (Shujah et al., 2022).

The agar well diffusion method was used to assess the antibacterial activity of pure and doped Al_2O_3 NSs against *E. coli*, as shown in Table 1 with a detailed depiction of combined isolates

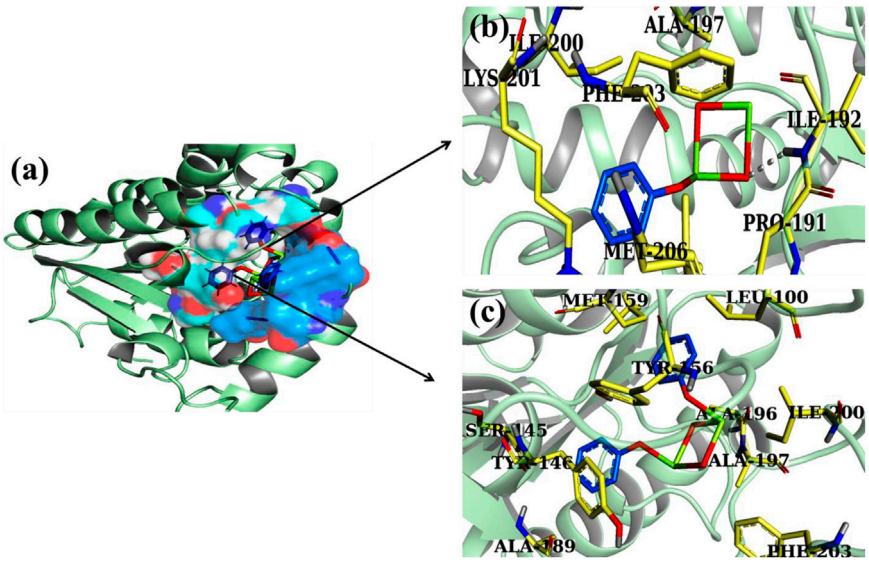

FIGURE 15
3D view of binding interaction of nanocomposites within the active site of $FabI_{E.coli}$ **(A)**, CS doped Al_2O_3 **(B)**, and GO/CS-doped Al_2O_3 **(C)**.

presented in Supplementary Table S2. *E. coli* displayed an inhibitory zone between (2.75 and 4.70 mm) and (3.95 and 5.65 mm) at low and high dosage concentrations. The quantification of the *E. coli* inhibition zone was compared to that of ciprofloxacin, which acted as the positive control with an inhibition zone measurement of 9.55 mm. DI-H_2O was used as the negative control, resulting in an inhibition zone measurement of 0 mm. Al_2O_3 and dopant materials showed maximum inhibitory zones when present in high concentrations. Figure 12A is the graphical representation of the inhibition zone measurement for antimicrobial analysis of pristine and GO/CS-doped Al_2O_3 NSs for the high and low inhibition zones when compared with ciprofloxacin. The % age efficacy for *E. coli* was calculated by dividing the sample's inhibition zone with the positive control inhibition area which increased 28.79%–49.21% and 41.36%–59.16% efficacy at low and high concentrations, correspondingly, as shown in Figure 12B.

Both the concentration and size of the particles have an impact on the antibacterial activity. Because of their smaller sizes, particles generate more reactive oxygen species (ROS). ROS causes cytoplasmic constituents to be extruded, which ultimately leads to the death of pathogens by way of penetration through the microorganism's membrane (Mustajab et al., 2022).

The mechanism underlying the bactericidal activity of prepared samples is reactive oxygen species (ROS), which generates oxidative stress on the bacterial cell wall (Ikram et al., 2022e).

$$Al_2O_3 + h\nu\,(\text{photon}) \rightarrow h^+\,(\text{hole}) + e^-\,(\text{excited electron})$$
$$e^- + O_2 \rightarrow {}^*O_2^-$$
$$h^+ + H_2O \rightarrow OH^- + H^+$$
$${}^*O_2^- + H^+ \rightarrow {}^*HO_2$$
$${}^*HO_2 + e^- + H^+ \rightarrow {}^*H_2O_2$$
$${}^*H_2O_2 + {}^*O_2^- \rightarrow {}^*OH + O_2 + OH^-$$

These species then encourage the extrusion of cytoplasmic components, which ultimately kill bacteria by breaching their membrane (Imani, 2011). The schematic diagram of the antibacterial mechanism is depicted in Figure 13.

The electron–hole pair is the main component in the emission of ROS. The ROS destroys the bacterial cell membrane mechanically, killing the organism (Imani, 2011). NSs attach to the cell wall like a helical, disorganized spring and penetrate the biological membranes, forming interlinks with the deoxyribonucleic acid (DNA) molecular structure. The functional groups of the components can directly connect with the phospholipids in the cell membrane if the permeability of the cell is increased along with the cytoplasmic leakage (Kasai et al., 2019). Cationic (Al^{+3}) interaction with the negatively charged cell membrane is another likely route for cell rupture, which ends in cell death (Mustajab et al., 2022).

Considerable research (Arularasu et al., 2020; Raza et al., 2021) has investigated the microbicidal potential of metal ion–containing nanoparticles and their ability to interact with bacteria through electrostatic, Van der Waals, or hydrophobic forces (Dakal et al., 2016; Shahzadi et al., 2022). The molecular analysis of the produced nanomaterials revealed their potential interactions with active site residues of specified enzyme targets as shown in Figure 14A. These nanocomposites exhibit modest binding energies toward DNA gyrase, demonstrating their crucial interaction with essential amino acids. Docked complexes exhibited H-bonds with Gly77, Arg76 (CS-doped Al_2O_3), and Gly77, and Thr165 (GO/CS-doped Al_2O_3) with binding scores of 2.98 and 3.34, as shown in Figures 14B, C, indicating its potential function as an inhibitor for DNA gyrase.

In $FabI_{E.coli}$, the produced nanocomposites exhibited identical binding patterns as shown in Figure 15A, with CS-doped Al_2O_3 exhibiting single H-bonds with the Ile192 amino acid of the active pocket and an overall crucial score of 2.90, as shown in Figure 15B. By contrast, GO/CS-doped Al_2O_3 exhibited a docked complex with

H-bonds inside the active site, namely, Thr156, Met159, and Ala196, and a binding score of 3.42 (Figure 15C).

In *silico* findings are comparable to the *in vitro* bactericidal activity against *E. coli*. CS-doped Al_2O_3 and its composites GO/CS-doped Al_2O_3 are potential inhibitors that require further exploration.

4 Conclusion

In this study, we successfully synthesized Al_2O_3, CS-doped Al_2O_3, and various concentrations (2 and 4 wt%) of GO/CS-doped Al_2O_3 via the sol–gel method. Various characterizations have been employed to investigate structural, morphological, and optical properties. The XRD analysis confirmed the tetragonal structure of aluminum oxide, with different composition phases appearing as $Al_{2\cdot67}O_4$ and Al_2O_3, indicating the polycrystalline nature of the synthesized nanoparticles. The crystalline size of the prepared pristine and GO/CS-doped NSs was calculated as 17.6, 24.8, 15.7, and 14.7 nm. The existence of the Al-O functional group was characterized by the FTIR analysis. The TEM analysis confirmed the morphology and topography of nanorods and quantum dots. The interlayer d-spacing was investigated using the HR-TEM analysis and measured as 0.24, 0.18, 0.23, and 0.23 nm for pristine and GO/CS-doped NSs. The elemental composition of the synthesized nanoparticles was analyzed through the EDS analysis, which confirmed the presence of both aluminum and oxygen. The catalytic degradation of the RhB dye was measured by using $NaBH_4$ as the reducing agent and GO/CS doped nanoparticles as a catalyst to enhance the reaction. The highest degradation was measured as 74.28, 76.57, and 81.11% for the acidic, basic, and neutral mediums. The 2% GO/CS-Al_2O_3 acted as a superior catalyst for the degradation of the RhB dye. The 2% GO/CS-Al_2O_3 enhanced the % degradation in all mediums because of increased active sites in the catalyst. The antimicrobial activity against *E. coli* was investigated by measuring the inhibition zones for low and high doses of NSs, that is, 4.70 and 5.65 mm. In *silico* predictions agree with the antibacterial activities against *E. coli* and suggest the given nanocomposites as possible inhibitors of β-lactamase and FabI.

Data availability statement

The original contributions presented in the study are included in the article/Supplementary Material; further inquiries can be directed to the corresponding author.

Author contributions

HZ: methodology, formal analysis, and writing—review and editing the manuscript; MIm: conceptualization and resources; AH: conceptualization, writing—review and editing the manuscript, and investigation; IS: data curation and resources; MM: investigation and data curation; AU-H: methodology and formal analysis; WN: formal analysis, conceptualization, and funding acquisition; FM: data analysis, interpretation, conceptualization, review and editing, investigation, formal analysis, and fund acquisition; SA: Investigation and review and editing; MIk: conceptualization, investigation, writing—original draft preparation of the manuscript, supervision, funding acquisition, and visualization.

Acknowledgments

The authors are thankful to HEC, Pakistan, through NRPU-20-17615 and express their gratitude for the support received from Universitat Rovira i Virgili under the Maria Zambrano Programme (reference number: 2021URV-MZ-10). Proyectos de Generación de Conocimiento AEI/MCIN (PID2021-123665OB-I00), and the project reference number of TED2021–129343B-I00.

Conflict of interest

The authors declare that the research was conducted in the absence of any commercial or financial relationships that could be construed as a potential conflict of interest.

Publisher's note

Supplementary material

The Supplementary Material for this article can be found online at: https://www.frontiersin.org/articles/10.3389/fenvs.2023.1180229/full#supplementary-material

References

Ahmad, A., Khan, N., Giri, B. S., Chowdhary, P., and Chaturvedi, P. (2020). Removal of methylene blue dye using rice husk, cow dung and sludge biochar: Characterization, application, and kinetic studies. *Bioresour. Technol.* 306, 123202. doi:10.1016/j.biortech.2020.123202

Ahn, K. S., Yan, Y., Shet, S., Jones, K., Deutsch, T., Turner, J., et al. (2008). ZnO nanocoral structures for photoelectrochemical cells. *Appl. Phys. Lett.* 93, 163117. doi:10.1063/1.3002282

Ali, M. H., Moon, M. M. A., and Rahman, M. F. (2019). Study of ultra-thin CdTe/CdS heterostructure solar cell purveying open-circuit voltage ~1.2 v. *Mater. Res. Express.* 6, 095515. doi:10.1088/2053-1591/ab3089

Altaf, S., Haider, A., Naz, S., Ul-Hamid, A., Haider, J., Imran, M., et al. (2020). Comparative study of selenides and tellurides of transition metals (Nb and Ta) with respect to its catalytic, antimicrobial, and molecular docking performance. *Nanoscale Res. Lett.* 15, 144. doi:10.1186/s11671-020-03375-0

Amirov, R. R., Shayimova, J., Nasirova, Z., and Dimiev, A. M. (2017). Chemistry of graphene oxide. Reactions with transition metal cations. *Carbon N. Y.* 116, 356–365. doi:10.1016/j.carbon.2017.01.095

Arularasu, M. V., Harb, M., and Sundaram, R. (2020). Synthesis and characterization of cellulose/TiO2 nanocomposite: Evaluation of *in vitro* antibacterial and *in silico* molecular docking studies. *Carbohydr. Polym.* 249, 116868. doi:10.1016/j.carbpol.2020.116868

Asada, T., Kayama, T., Kusaba, H., Einaga, H., and Teraoka, Y. (2008). Preparation of alumina-supported LaFeO3 catalysts and their catalytic activity

for propane combustion. *Catal. Today*. 139, 37–42. doi:10.1016/j.cattod.2008.08.006

Atrak, K., Ramazani, A., and Taghavi Fardood, S. (2018). Green synthesis of amorphous and gamma aluminum oxide nanoparticles by tragacanth gel and comparison of their photocatalytic activity for the degradation of organic dyes. *J. Mater. Sci. Mater. Electron*. 29, 8347–8353. doi:10.1007/s10854-018-8845-2

Baqir, M. A., Farmani, A., Raza, M., Akhtar, M. N., and Hussain, A. (2021). Engineering of metallic nanorod-based hyperbolic metamaterials for broadband applications operating in the infrared regime. *Appl. Nanosci.* 11, 229–240. doi:10.1007/s13204-020-01574-w

Bari, A., Ikram, M., Haider, A., Ul-Hamid, A., Haider, J., Shahzadi, I., et al. (2022). Evaluation of bactericidal potential and catalytic dye degradation of multiple morphology based chitosan/polyvinylpyrrolidone-doped bismuth oxide nanostructures. *Nanoscale Adv.* 4, 2713–2728. doi:10.1039/d2na00105e

Bauer, A. W., Kirby, W. M., Sherris, J. C., and Turck, M. (1966). Antibiotic susceptibility testing by a standardized single disk method. *Am. J. Clin. Pathol.* 45, 493–496. doi:10.1093/ajcp/45.4_ts.493

Bhattacharya, S., Saha, I., Mukhopadhyay, A., Chattopadhyay, D., and Chand, U. (2013). Role of nanotechnology in water treatment and purification: Potential applications and implications. *Int. J. Chem. Sci. Technol.* 3, 59–64. Available at: https://www.academia.edu/download/51031736/Role_of_nanotechnology_in_water_treatmen20161223-22148-dx9shz.pdf.

Bilal, M., Ikram, M., Shujah, T., Haider, A., Naz, S., Ul-Hamid, A., et al. (2022). Chitosan-Grafted polyacrylic acid-doped copper oxide nanoflakes used as a potential dye degrader and antibacterial agent: *In silico* molecular docking analysis. *ACS Omega* 7, 41614–41626. doi:10.1021/acsomega.2c05625

Bu, Y., Chen, Z., Li, W., and Hou, B. (2013). Highly efficient photocatalytic performance of graphene-ZnO quasi-shell-core composite material. *ACS Appl. Mater. Interfaces*. 5, 12361–12368. doi:10.1021/am403149g

Cintrón, M. S., and Hinchliffe, D. J. (2015). FT-IR examination of the development of secondary cell wall in cotton fibers. *Fibers* 3, 30–40. doi:10.3390/fib3010030

Costina, I., and Franchy, R. (2001). Band gap of amorphous and well-ordered Al2O3 on Ni3Al(100). *Appl. Phys. Lett.* 78, 4139–4141. doi:10.1063/1.1380403

Dakal, T. C., Kumar, A., Majumdar, R. S., and Yadav, V. (2016). Mechanistic basis of antimicrobial actions of silver nanoparticles. *Front. Microbiol.* 7, 1831. doi:10.3389/fmicb.2016.01831

Datta, S., Veena, R., Samuel, M. S., and Selvarajan, E. (2021). Immobilization of laccases and applications for the detection and remediation of pollutants: A review. *Environ. Chem. Lett.* 19, 521–538. doi:10.1007/s10311-020-01081-y

Deveci, İ., and Mercimek, B. (2019). Performance of SiO2/Ag Core/Shell particles in sonocatalalytic degradation of Rhodamine B. *Ultrason. Sonochem.* 51, 197–205. doi:10.1016/j.ultsonch.2018.10.025

Feuerstein, A., Scuda, N., Klose, C., Hoffmann, A., Melchner, A., Boll, K., et al. (2022). Antimicrobial resistance, serologic and molecular characterization of *E. coli* isolated from calves with severe or fatal enteritis in Bavaria, Germany. *Antibiotics* 11, 23. doi:10.3390/antibiotics11010023

Gadgil, A. (1998). Drinking water in developing countries. *Annu. Rev. Energy Environ.* 23, 253–286. doi:10.1146/annurev.energy.23.1.253

Gao, T., Yu, J., Zhou, Y., and Jiang, X. (2017). The synthesis of graphene oxide functionalized with dithiocarbamate group and its prominent performance on adsorption of lead ions. *J. Taiwan Inst. Chem. Eng.* 71, 426–432. doi:10.1016/j.jtice.2016.11.033

Ge, W., Liu, X., Ye, J., Li, Q., Jiang, H., and Wang, X. (2015). Green photochemical synthesis of fluorescent carbon spheres *in-situ* enwrapped around Ag nanoparticles. *Sci. China Chem.* 58, 634–639. doi:10.1007/s11426-014-5254-0

Gordani, G. R., Loghman Estarki, M. R., Danesh, M., Kiani, E., and Tavoosi, M. (2022). Microstructure, phase, magnetic properties, and electromagnetic wave absorption of graphene oxide – Ni0.7Zn0.3Fe2O4 – Al2O3 aerogel. *Ceram. Int.* 48, 3059–3069. doi:10.1016/j.ceramint.2021.10.081

Haider, A., Ijaz, M., Ali, S., Haider, J., Imran, M., Majeed, H., et al. (2020). Green synthesized phytochemically (zingiber officinale and allium sativum) reduced nickel oxide nanoparticles confirmed bactericidal and catalytic potential. *Nanoscale Res. Lett.* 15, 50. doi:10.1186/s11671-020-3283-5

Haider, A., Ijaz, M., Imran, M., Naz, M., Majeed, H., Khan, J. A., et al. (2020). Enhanced bactericidal action and dye degradation of spicy roots' extract-incorporated fine-tuned metal oxide nanoparticles. *Appl. Nanosci.* 10, 1095–1104. doi:10.1007/s13204-019-01188-x

Holder, S. L., Lee, C. H., and Popuri, S. R. (2017). Simultaneous wastewater treatment and bioelectricity production in microbial fuel cells using cross-linked chitosan-graphene oxide mixed-matrix membranes. *Environ. Sci. Pollut. Res.* 24, 13782–13796. doi:10.1007/s11356-017-8839-2

Ikram, M., Abid, N., Haider, A., Ul-Hamid, A., Haider, J., Shahzadi, A., et al. (2022). Toward efficient dye degradation and the bactericidal behavior of Mo-doped La2O3nanostructures. *Nanoscale Adv.* 4, 926–942. doi:10.1039/d1na00802a

Ikram, M., Ali, S., Aqeel, M., Ul-Hamid, A., Imran, M., Haider, J., et al. (2020). Reduced graphene oxide nanosheets doped by Cu with highly efficient visible light photocatalytic behavior. *J. Alloys Compd.* 837, 155588. doi:10.1016/j.jallcom.2020.155588

Ikram, M., Haider, A., Imran, M., Haider, J., Naz, S., Ul-Hamid, A., et al. (2022). Facile synthesis of starch and tellurium doped SrO nanocomposite for catalytic and antibacterial potential: *In silico* molecular docking studies. *Int. J. Biol. Macromol.* 221, 496–507. doi:10.1016/j.ijbiomac.2022.09.034

Ikram, M., Inayat, T., Haider, A., Ul-Hamid, A., Haider, J., Nabgan, W., et al. (2021). Graphene oxide-doped MgO nanostructures for highly efficient dye degradation and bactericidal action. *Nanoscale Res. Lett.* 16, 56. doi:10.1186/s11671-021-03516-z

Ikram, M., Rasheed, F., Haider, A., Naz, S., Ul-Hamid, A., Shahzadi, A., et al. (2022). Photocatalytic and antibacterial activity of graphene oxide/cellulose-doped TiO2 quantum dots: In silico molecular docking studies. *Nanoscale Adv.* 4, 3764–3776. doi:10.1039/d2na00383j

Ikram, M., Raza, A., Imran, M., Ul-Hamid, A., Shahbaz, A., and Ali, S. (2020). Hydrothermal synthesis of silver decorated reduced graphene oxide (rGO) nanoflakes with effective photocatalytic activity for wastewater treatment. *Nanoscale Res. Lett.* 15, 95. doi:10.1186/s11671-020-03323-y

Ikram, M., Saeed, M., Haider, J., Haider, A., Ul-Hamid, A., Shahzadi, A., et al. (2022). Facile synthesis of chitosan-grafted polyacrylic acid-doped CaO nanoparticle for catalytic and antimicrobial potential. *Appl. Nanosci.* 12, 2657–2670. doi:10.1007/s13204-022-02576-6

Ikram, M., Shahzadi, A., Hayat, S., Nabgan, W., Ul-Hamid, A., Haider, A., et al. (2022). Novel Ta/chitosan-doped CuO nanorods for catalytic purification of industrial wastewater and antimicrobial applications. *RSC Adv.* 12, 16991–17004. doi:10.1039/d2ra03006c

Iwalokun, B. A., Ogunledun, A., Ogbolu, D. O., Bamiro, S. B., and Jimi-Omojola, J. (2004). *In vitro* antimicrobial properties of aqueous garlic extract against multidrug-resistant bacteria and Candida species from Nigeria. *J. Med. Food.* 7, 327–333. doi:10.1089/jmf.2004.7.327

Jaishankar, M., Tseten, T., Anbalagan, N., Mathew, B. B., and Beeregowda, K. N. (2014). Toxicity, mechanism and health effects of some heavy metals. *Interdiscip. Toxicol.* 7, 60–72. doi:10.2478/intox-2014-0009

Jamal, F., Ikram, M., Haider, A., Ul-Hamid, A., Ijaz, M., Nabgan, W., et al. (2022). Facile synthesis of silver and polyacrylic acid doped magnesium oxide nanostructure for photocatalytic dye degradation and bactericidal behavior. *Appl. Nanosci.* 12, 2409–2419. doi:10.1007/s13204-022-02504-8

Javaid, R., and Qazi, U. Y. (2019). Catalytic oxidation process for the degradation of synthetic dyes: An overview. *Int. J. Environ. Res. Public Health.* 16, 2066. doi:10.3390/ijerph16112066

Jiao, W. Q., Yue, M. B., Wang, Y. M., and He, M. Y. (2012). Synthesis of morphology-controlled mesoporous transition aluminas derived from the decomposition of alumina hydrates. *Microporous Mesoporous Mater* 147, 167–177. doi:10.1016/j.micromeso.2011.06.012

Jirátová, K., and Beránek, L. (1982). Properties of modified aluminas. *Appl. Catal.* 2, 125–138. doi:10.1016/0166-9834(82)80196-6

Kasai, D., Chougale, R., Masti, S., Chalannavar, R., Malabadi, R. B., Gani, R., et al. (2019). An investigation into the influence of filler piper nigrum leaves extract on physicochemical and antimicrobial properties of chitosan/poly (vinyl alcohol) blend films. *J. Polym. Environ.* 27, 472–488. doi:10.1007/s10924-018-1353-x

Khan, A. D., Ikram, M., Haider, A., Ul-Hamid, A., Nabgan, W., and Haider, J. (2022). Polyvinylpyrrolidone and chitosan-doped lanthanum oxide nanostructures used as anti-bacterial agents and nano-catalyst. *Appl. Nanosci.* 12, 2227–2239. doi:10.1007/s13204-022-02471-0

Mahmoud, S. A., Elsisi, M. E., and Mansour, A. F. (2022). Synthesis and electrochemical performance of α-Al2O3 and M-Al2O4 spinel nanocomposites in hybrid quantum dot-sensitized solar cells. *Sci. Rep.* 12, 17009. doi:10.1038/s41598-022-21186-4

Mehmood, Z., Ikram, M., Imran, M., Shahzadi, A., Haider, A., Ul-Hamid, A., et al. (2022). Z. officinale-doped silver/calcium oxide nanocomposites: Catalytic activity and antimicrobial potential with molecular docking analysis. *Process Biochem.* 121, 635–646. doi:10.1016/j.procbio.2022.07.035

Moeen, S., Ikram, M., Haider, A., Haider, J., Ul-Hamid, A., Nabgan, W., et al. (2022). Comparative study of sonophotocatalytic, photocatalytic, and catalytic activities of magnesium and chitosan-doped tin oxide quantum dots. *ACS Omega* 7, 46428–46439. doi:10.1021/acsomega.2c05133

Montes-Navajas, P., Asenjo, N. G., Santamaría, R., Menéndez, R., Corma, A., and García, H. (2013). Surface area measurement of graphene oxide in aqueous solutions. *Langmuir* 29, 13443–13448. doi:10.1021/la4029904

Mustajab, M., Ikram, M., Haider, A., Ul-Hamid, A., Nabgan, W., Haider, J., et al. (2022). Promising performance of polyvinylpyrrolidone-doped bismuth oxyiodide quantum dots for antibacterial and catalytic applications. *Appl. Nanosci.* 12, 2621–2633. doi:10.1007/s13204-022-02547-x

Naika, H. R., Lingaraju, K., Manjunath, K., Kumar, D., Nagaraju, G., Suresh, D., et al. (2015). Green synthesis of CuO nanoparticles using Gloriosa superba L. extract and their antibacterial activity. *J. Taibah Univ. Sci.* 9, 7–12. doi:10.1016/j.jtusci.2014.04.006

NCCLS (2007). Performance standards for antimicrobial susceptibility testing. *Clin. Lab. Standars Inst. - NCCLS.* 27, 1–182. Available at: https://agris.fao.org/agris-search/search.do?recordID=US201300057088.

Niu, M., Ying, Y., Bartell, P. A., and Harvatine, K. J. (2017). The effects of feeding rations that differ in fiber and fermentable starch within a day on milk production and the daily rhythm of feed intake and plasma hormones and metabolites in dairy cows. *J. Dairy Sci.* 100, 187–198. doi:10.3168/jds.2016-11129

Omanwar, S. K., Jaiswal, S. R., Bhatkar, V. B., and Koparkar, K. A. (2018). Comparative study of nano-sized Al2O3 powder synthesized by sol-gel (citric and stearic acid) and aldo-keto gel method. *Opt. (Stuttg)* 158, 1248–1254. doi:10.1016/j.ijleo.2017.12.068

Panchaud, P., Bruyère, T., Blumstein, A. C., Bur, D., Chambovey, A., Ertel, E. A., et al. (2017). Discovery and optimization of isoquinoline ethyl ureas as antibacterial agents. *J. Med. Chem.* 60, 3755–3775. doi:10.1021/acs.jmedchem.6b01834

Penner, M. H. (2017). "Ultraviolet, visible, and fluorescence spectroscopy," in *Food analysis* (Berlin: Springer Science & Business Media), 89–106. doi:10.1007/978-3-319-45776-5_7

Rafiq, A., Ikram, M., Ali, S., Niaz, F., Khan, M., Khan, Q., et al. (2021). Photocatalytic degradation of dyes using semiconductor photocatalysts to clean industrial water pollution. *J. Ind. Eng. Chem.* 97, 111–128. doi:10.1016/j.jiec.2021.02.017

Rahman, Q. I., Ahmad, M., and Mehta, S. K. (2017). Hydrothermal synthesis of Cr-doped SrTiO3 nanoparticles for rhodamine-B dye degradation under visible light illumination. *Colloid Polym. Sci.* 295, 933–937. doi:10.1007/s00396-017-4085-x

Rahman, Q. I., Ahmad, M., Misra, S. K., and Lohani, M. (2013). Effective photocatalytic degradation of rhodamine B dye by ZnO nanoparticles. *Mater. Lett.* 91, 170–174. doi:10.1016/j.matlet.2012.09.044

Raza, A., Hassan, J. Z., Ikram, M., Naz, S., Haider, A., Ul-Hamid, A., et al. (2021). Molecular docking and DFT analyses of magnetic cobalt doped MoS2 and BN nanocomposites for catalytic and antimicrobial explorations. *Surfaces Interfaces* 27, 101571. doi:10.1016/j.surfin.2021.101571

Said, A. E.-A. A., El-Wahab, M. M. M. A., and El-Aal, M. A. (2016). The role of acid sites in the catalytic performance of tungsten oxide during the dehydration of isopropyl and methyl alcohols. *Chem. Mater. Eng.* 4, 17–25. doi:10.13189/cme.2016.040202

Seefeld, M. A., Miller, W. H., Newlander, K. A., Burgess, W. J., DeWolf, W. E., Elkins, P. A., et al. (2003). Indole naphthyridinones as inhibitors of bacterial enoyl-ACP reductases FabI and FabK. *J. Med. Chem.* 46, 1627–1635. doi:10.1021/jm0204035

Shahzadi, I., Islam, M., Saeed, H., Haider, A., Shahzadi, A., Haider, J., et al. (2022). Formation of biocompatible MgO/cellulose grafted hydrogel for efficient bactericidal and controlled release of doxorubicin. *Int. J. Biol. Macromol.* 220, 1277–1286. doi:10.1016/j.ijbiomac.2022.08.142

Sharma, S., Kumar, K., Thakur, N., Chauhan, S., and Chauhan, M. S. (2020). The effect of shape and size of ZnO nanoparticles on their antimicrobial and photocatalytic activities: A green approach. *Bull. Mater. Sci.* 43, 20. doi:10.1007/s12034-019-1986-y

Shujah, T., Shahzadi, A., Haider, A., Mustajab, M., Haider, A. M., Ul-Hamid, A., et al. (2022). Molybdenum-doped iron oxide nanostructures synthesized via a chemical co-precipitation route for efficient dye degradation and antimicrobial performance: In silico molecular docking studies. *RSC Adv.* 12, 35177–35191. doi:10.1039/d2ra07238f

Imani, S. (2011). International Journal of Nano Dimension Determining the antibacterial effect of ZnO nanoparticle against the pathogenic bacterium. *Shigella dysenteriae* 1, 279–285. (type 1). Available at: https://www.sid.ir/EN/VEWSSID/J_pdf/1010420110406.pdf.

Sinclair, C. G. (1939). Bergey's manual of determinative Bacteriology. *Am. J. Trop. Med. Hyg.* s1-19, 605–606. doi:10.4269/ajtmh.1939.s1-19.605

Tju, H., Shabrany, H., Taufik, A., and Saleh, R. (2017). Degradation of methylene blue (MB) using ZnO/CeO2/nanographene platelets (NGP) photocatalyst: Effect of various concentration of NGP. *AIP Conf. Proc.* 1862, 030037. American Institute of Physics Inc. doi:10.1063/1.4991141

Ullah, H., Viglašová, E., and Galamboš, M. (2021). Visible light-driven photocatalytic rhodamine B degradation using CdS nanorods. *Processes* 9, 263. doi:10.3390/pr9020263

Vijayan, R., Joseph, S., and Mathew, B. (2019). Green synthesis of silver nanoparticles using *Nervalia zeylanica* leaf extract and evaluation of their antioxidant, catalytic, and antimicrobial potentials. *Sci. Technol.* 37, 809–819. doi:10.1080/02726351.2018.1450312

Wang, Z., Wu, A., Ciacchi, L. C., and Wei, G. (2018). Recent advances in nanoporous membranes for water purification. *Nanomaterials* 8, 65. doi:10.3390/nano8020065

World Health Organization (2003). Emerging issues in water and infectious disease world health organization. Available at: https://apps.who.int/iris/bitstream/handle/10665/42751/9241590823.pdf.

Yilmaz, M., Mengelizadeh, N., khodadadi Saloot, M., Shahbaksh, S., and Balarak, D. (2022). Facile synthesis of Fe3O4/ZnO/GO photocatalysts for decolorization of acid blue 113 under solar, visible and UV lights. *Mater. Sci. Semicond. process.* 144, 106593. doi:10.1016/j.mssp.2022.106593

Yuan, X., Zhu, J., Tang, K., Cheng, Y., Xu, Z., and Yang, W. (2015). Formation and properties of 1-D alumina nanostructures prepared via a template-free thermal reaction. *Procedia Eng.* 102, 602–609. Elsevier Ltd. doi:10.1016/j.proeng.2015.01.135

Zhu, Q., Lu, J., Wang, Y., Qin, F., Shi, Z., and Xu, C. (2016). Burstein-moss effect behind Au surface plasmon enhanced intrinsic emission of ZnO microdisks. *Sci. Rep.* 6, 36194. doi:10.1038/srep36194